Lab on a Chip

COMMUNICATION

View Article Online
View Journal | View Issue

Check for updates

Cite this: *Lab Chip*, 2022, **22**, 40

Received 26th August 2021,
Accepted 1st October 2021

DOI: 10.1039/d1lc00758k

rsc.li/loc

Droplet-assisted electrospray phase separation using an integrated silicon microfluidic platform†

Yan Zhang,[a] Sungho Kim,[a] Weihua Shi,[a] Yaoyao Zhao,[b] Insu Park,[c] Christopher Brenden,[c] Hrishikesh Iyer,[a] Prasoon Jha,[a] Rashid Bashir,[c] Jonathan V. Sweedler[b] and Yurii Vlasov*[ac]

We report a silicon microfluidic platform that enables monolithic integration of transparent micron-scale microfluidic channels, an on-chip segmentation of analyte flows into picoliter-volume droplets, and a nano-electrospray ionization emitter that enables spatial and temporal separation of oil and aqueous phases during electro-spray for subsequent mass spectrometry analysis.

Introduction

Coupling of droplet microfluidics with nano-electrospray ionization mass spectrometry (nESI-MS) is a promising platform for high-throughput, label-free, multiplexed analysis with improved temporal and chemical sensitivity.[1] Segmentation of water-dissolved analytes flowing in microfluidic channels into a series of oil-isolated plugs enables precise control of chemical reactions in these femto- to nanoliter volume reaction chambers.[2,3] Hence, due to these advantages, droplet-assisted nESI-MS has been explored for single-cell chemical analysis,[4] biocatalysis,[3,5] proteomics,[6] screening of enzyme libraries,[7] high-throughput analysis,[8] surface sampling,[9] and was shown to be promising as a rapid biomarker screening tool for clinical diagnostics.[10] Since Taylor dispersion[11] is halted, the band broadening due to longitudinal diffusion is minimized, which enables droplet-by-droplet kinetic studies of chemical reactions.

Of specific interest in this respect is the application of droplet microfluidics to *in vivo* sampling of various neurochemicals from the brain,[12–20] since temporally resolving fast changes in neurochemical concentrations is important to understanding the functionality of brain circuits. For example, using droplet-assisted nESI-MS, acetylcholine in dialysate droplets (160 nL) was monitored with 5 s temporal resolution and a limit of detection (LOD) of 5 nM.[21] Further performance improvement is envisioned by decreasing the droplet volume into the sub-nL regime, decreasing flow rates below μL min^{-1}, and improving delivery and ionization efficiency of the analytes in nESI-MS by miniaturization of microfluidic components and their integration into a single chip-scale system.[22] Here we developed such a monolithic silicon microfluidic platform that generates pL-volume droplets and efficiently delivers them to nESI-MS for high-throughput and highly sensitive chemical analysis.

While sample preparation in a droplet-assisted nESI-MS is greatly facilitated by the flexibility and precise control provided by droplet microfluidics, however, efficient coupling of segmented microfluidic flows to nESI-MS is far from trivial. The appearance of an immiscible carrier fluid at the nESI orifice often disrupts the formation of a Taylor cone resulting in enhanced instability of the MS signal. Moreover, the electrospray of the oil phase, which is often composed of fluorous or mineral oils accompanied by surfactants, can result in sequestration of charge carriers thus compromising the ionization efficiency of the aqueous phase. To overcome these limitations, several methods have been proposed to separate the aqueous phase from the oil carrier before the infusion to nESI-MS. Electro-coalescence of aqueous droplets into a continuous aqueous flow has been achieved by the application of time-coordinated electrical pulses.[23] However, this also leads to significant sample dilution in the transferring line, increased flow rates, and sample zone spreading that reduces ionization efficiencies and temporal resolution. Dilution-free extraction of the aqueous phase from a segmented flow has been demonstrated by modulating interfacial tension to facilitate droplet merging prior to delivery to nESI-MS. This mechanism was utilized by the integration of an array of

---

[a] *Department of Electrical and Computer Engineering, University of Illinois Urbana Champaign, IL 61801, USA. E-mail: yvlasov@illinois.edu*
[b] *Department of Chemistry and the Beckman Institute, University of Illinois Urbana Champaign, IL 61801, USA*
[c] *Department of Bioengineering, University of Illinois Urbana Champaign, IL 61801, USA*

† Electronic supplementary information (ESI) available: Background-subtracted video of temporal and spatial phase separation during electrospray. 2Mb GIF file. See DOI: 10.1039/d1lc00758k

micron-scale cylindrical posts,[24] incorporation of spatially selective hydrophilic surface coatings,[25] or by using a hydrophilic extraction bridge.[26] The efficient draining of the oil phase has been also achieved by adding a hydrophobic Teflon-based capillary right below the orifice of nESI emitter tip.[2,27] Most of these approaches, however, are difficult to extend to sub-nL volume droplets and low flow rate down to nL min^{-1}, while achieving monolithic chip-scale integration.

In this paper, we introduce an approach to enhance performance by the design and characterization of a silicon-integrated miniaturized microfluidic platform containing ultra-small 7 μm-radius microfluidic channels to support ultra-slow nL min^{-1} flow rates. The chip also integrates a T-junction droplet generator capable of producing pL-scale droplets and a novel nESI emitter that can spatially and temporally separate oil and aqueous phases on a droplet-by-droplet basis during electrospray.

Silicon microfluidic platform

While silicon was used at the dawn of microfluidics research, the majority of later efforts have been shifted to development of microfluidic devices based on polymers,[28] most notably on polydimethylsiloxane (PDMS), mostly due to the much simpler and cost-effective fabrication using soft lithography approaches. Recently, there is a renewed interest in using silicon for microfluidic devices and systems[15,20,22,29–34] dictated by tremendous progress in microelectronics fabrication technologies that enable lithographic control of feature size at the scale of just a few nanometers. With mass production and availability of foundry services, the cost of silicon chips has decreased exponentially during the last few decades and has become comparable with the cost efficiency of soft lithography approaches.

In traditional glass or polymer-based microfluidic chips, the hydrodynamic channel cross-section is of the order of thousands of μm^2 with typical flow rates around several μL min^{-1}. While it is possible to generate sub-nL volume oil-segmented aqueous flows in PDMS-based microfluidics by decreasing the channel cross-section and flow rates, stabilizing monodisperse droplet generation becomes increasingly challenging. This is mostly due to the inability of PDMS that has a very low (~1 MPa) Young's modulus to maintain constant volume of microfluidic channels during large pressure fluctuations related to the droplet generation cycle. Glass (Young's modulus of 50 GPa) can provide better control of pressures and flows to generate oil-segmented aqueous droplets of picoliter volume. In contrast to glass- or polymer-based platforms, silicon-based microfabrication offers a large Young's modulus, precise lithographic control, and the ability to locally dope the silicon substrate to enable local concentration of electric fields. This makes it very attractive for applications such as nESI.

As opposed to many silicon fabrication approaches that produce microfluidic channels buried deeply in the silicon wafer using deep reactive ion etching (DRIE)[34] or wafer bonding technologies,[31] here we aim at fabricating shallow channels sealed from the top surface with a silicon nitride (SiN$_x$) cover. The resulting channels are optically transparent for visible light and can be readily visualized with standard fluorescence microscopy. For stable control of ultra-slow segmented flows, we aim for channel cross-sections of just a few tens of μm^2 that are 100× smaller than in typical droplet microfluidics systems. We also aim at minimizing the thickness of silicon substrate from the typical hundreds of microns to just a few tens of microns to further localize the electric fields for efficient n-ESI, as well as to minimize the tissue damage if such probes are used for neurochemical sensing in the brain. To achieve all of these objectives, we have developed a silicon-on-insulator (SOI) platform (Fig. 1) that enables stable generation of monodisperse pL-volume oil-separated aqueous plugs with ultra-slow nL min^{-1} flow rates at a few Hz frequencies,[32] while offering monolithic integration of various microfluidic components on a single miniaturized chip.

Fabrication

The SOI integrated microfluidic chips (Fig. 1) are fabricated on an SOI wafer with a 15 μm-thick device layer (B-doped, 0.005 Ω cm) and 0.5 μm-thick buried oxide layer. Fabrication is divided into two stages: microfluidic channel formation, and definition of the suspended silicon nESI cantilever (Fig. 1). First, a 0.3 μm-thick SiN$_x$ layer is deposited using plasma enhanced chemical vapor deposition (PECVD) on top of the SOI device layer to serve as a hard mask. To form the microfluidic channels, a series of 1 μm-diameter holes are first defined by direct laser writing lithography (Heidelberg μPG 101) and then etched through the SiN$_x$ layer by inductively coupled plasma reactive ion etching (ICP-RIE). Subsequent isotropic silicon etching with XeF$_2$ forms connected buried microfluidic channels with a radius of 7 μm (Fig. 1A and D). The fabricated channels are then sealed

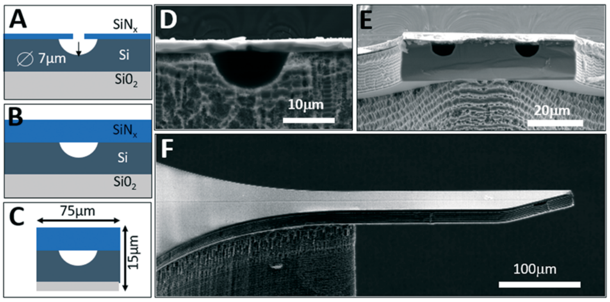

Fig. 1 SOI microfluidic fabrication platform. A) Schematic cross-section of an SOI wafer with lithographically defined holes in the SiN$_x$ hard mask that are used to isotropically etch microfluidic channels. B) Sealing of the buried channels by deposition of an additional SiN$_x$ layer. C) Series of DRIE steps define the suspended nESI emitter. D) SEM view of a device cross-section showing the buried microfluidic channel of 7 μm radius. E) Cross-section of the released SOI emitter cantilever. F) Side-view of the suspended emitter cantilever with lithographically defined nozzle.

from the top by PECVD of a 4 μm-thick stress-free silicon nitride layer (Fig. 1B and E). Next, the shape of the nESI emitter is defined by contact lithography to perform ICP-RIE etching to remove SiN_x at the perimeter of the cantilever followed by DRIE etching through the silicon device layer down to the buried oxide. The third lithography step and DRIE etching are used to etch through the handle silicon layer from the backside that releases the suspended nESI emitter cantilever with a final cross-section of just 15 × 75 μm^2 (Fig. 1C and F). As opposed to previous work on SOI-based nESI emitters employing open-channel capillary forces for controlling the analyte flow,[29] our platform employs sealed channels that provide superior control of flow rates.

Design of nESI nozzle

Our SOI fabrication platform enables precise and independent control of the microfluidic channels and the emitter nozzle geometry as they are defined by two separate lithography levels. In our design, (Fig. 2) besides defining nozzle shape at a μm-scale that is beneficial for electrospray control,[30,33] we also use doping of the SOI device layer to enable strong localization of electric field. Our first design (Fig. 2A and D) is a symmetric sharpened nozzle with an outlet orifice positioned right at the nozzle tip. COMSOL numerical simulations for a heavily doped (10^{18} cm^{-3}) silicon nozzle reveal a single electric field "hot spot" localized within just 25 μm of the emitter nozzle. With 2 kV applied between the silicon emitter nozzle and a metal plate located 2 mm away, the electric field strength in the "hot spot" approaches 60 kV cm^{-1}. The second design (Fig. 2B and E) with a flat nozzle moves a pair of "hot spots" 30 μm laterally, away from the outlet orifice. However, the axial symmetry of this design results in a "hot spot" electric field strength dropped by a factor of 2. The third design with an angled nozzle (Fig. 2C and F) breaks the symmetry with a leftmost stronger "hot spot" restored to 55 kV cm^{-1}. Our design approach here is based on a strong intuition that when the oil-segmented flow is ejected at the outlet orifice, electrospray of oil and aqueous phases will have different dynamics. While the formation of an aqueous Taylor cone can be achieved at relatively low electric field strength, the initiation of electrospraying of the neutral oil phase typically requires much higher electric fields. Since the electric field "hot spots" in our designs 2 and 3 are moved outside of the immediate outlet orifice, the oil phase will have some time to expand towards the sharpened nozzle edges prior to electrospraying (see inset in Fig. 2G). In this model it can be derived that the time required for the oil phase to reach the nozzle edges (and to be removed from the tip by electrospraying) is defined by the following equation:

$$t = \frac{3\pi R}{U}\left(\frac{\theta W^2}{4\sin^2\theta} - \frac{W^2}{4\tan\theta}\right), \qquad (1)$$

where R is the channel radius, U is the volumetric flow rate, θ represents the contact angle of the oil phase to a nozzle sidewall, and W denotes nozzle width. For illustrative curves in Fig. 2G, the channel radius R is assumed to be 5 μm, and oil contact angle θ is 45°. Contour lines correspond to a specific time required for the oil phase to reach the nozzle edges and to be removed by electrospraying. Increasing the oil flow rate U will result in faster arrival of oil fronts to the nozzle edges, while increasing of the nozzle width W will result in longer arrival time. Accordingly, to avoid accumulation of oil in-between segmented flow cycles, droplet frequency (hence sampling time resolution) is limited by the nozzle width and the flow rate. Following constant time contour plots in Fig. 2G, our designs 2 and 3 of Fig. 2B–F with the nozzle width of 75 μm should support electrospraying of an oil-segmented flow at frequencies of 1 Hz and faster (faster than 1 s time resolution sampling) at flow rates over 1 nL min^{-1}.

On-chip integration

Our platform is amenable for dense on-chip integration of many other microfluidic devices, such as droplet generators,

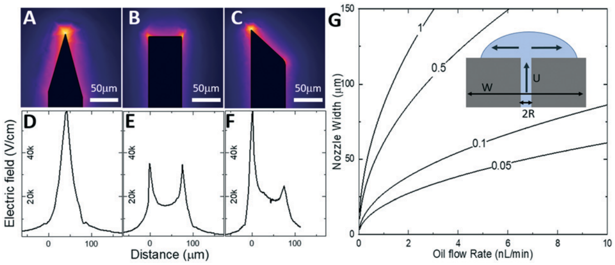

Fig. 2 Design principle for the nESI emitter nozzle for phase separation. Numerical COMSOL calculations of electric field distribution for three designs of the nESI nozzle geometry. A)–C) Top-down map of the electric field strength. Colour coding is in logarithmic scale. Electric field "hot spots" appear at the probe extremities. D)–F) Calculated profiles of electric field distribution (in units of kV cm^{-1}) along the surface of the nozzle. G) Design parameters of the nESI tip based on eqn (1): contours of constant time (in s) required for oil to reach the left and right edges of the tip (and removal by electrospray) as a function of the width W of the nozzle and oil flow rate U.

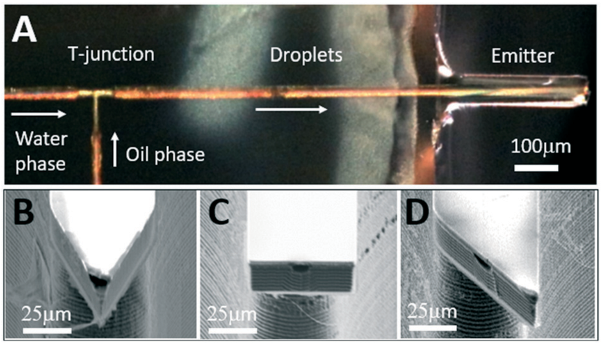

Fig. 3 Fabrication of the silicon microfluidic integrated chip. A) Top-down optical microscope image of the integrated microfluidic system featuring oil-phase and water-phase microfluidic channels, a T-junction for droplet generation, and the nESI emitter with the flat end (design 2). B)–D) Front-view SEM images of various designs of the nozzle geometry.

delay lines, mixers, and packaging structures, together with the nESI emitter since no additional lithography levels or fabrication steps are required. Fig. 3A illustrates an example of such dense on-chip integration featuring a microfluidic system with oil-phase and water-phase microfluidic channels, a T-junction for droplet generation, the nESI emitter with flat end (design 2), and inlet/outlet in-plane stubs (not shown) for external plumbing.

To characterize the influence of various designs of the nESI emitter nozzle of Fig. 2 on the electrospray of oil-segmented aqueous flows, a series of silicon chips were fabricated that integrate the various nozzle designs of the emitter cantilever (Fig. 3B–D).

On-chip droplet generation

Since we scaled down the channel cross-section by 100×, the flow rates need to be scaled accordingly to ensure generation of monodisperse droplets in a squeezing regime.[35] As opposed to natively hydrophobic PDMS-based surfaces (water contact angle larger than 100°), the internal surface of our microfluidic channels is hydrophilic as it is formed by either native silicon oxide or deposited silicon nitride. Numerical simulations by COMSOL (Fig. 4A) indicate that when the oil phase (1-octanol) is injected at the orthogonal T-junction into a continuous aqueous phase, a series of pL-volume oil droplets are formed in a stable squeezing regime at modest flow rate ratios of 2–10. Experimentally, since the microfluidic channels are located at the chip surface and sealed with a transparent SiN_x layer, standard methods of flow visualization using various dyes and fluorescence optical microscopy can be used. To control the flow rate of continuous aqueous phase (fluorescein in DI water) and dispersed oil phase (1-octanol, Sigma-Aldrich), a pressure pump (Flow-EZ, LUFEZ7000, Fluigent) and syringe pump (11 Pico Plus Elite, Harvard Apparatus) were used. An inverted fluorescence microscope (IX73, Olympus) equipped with a PMT detector (PMT 2101, Thorlabs) and a video camera (Hero 8, GoPro operated at 30–240 fps) were used to quantify droplet volume and frequency. Videography of the meniscus shape during droplet formation at the T-junction (Fig. 4B) confirms operation in a squeezing regime and generation of monodisperse pL-volume oil droplets with ultra-slow flow rates of just a few nL min^{-1}, which is beneficial for increased sensitivity of ESI-based mass spectrometry.[36] Variation of flow rate ratios between aqueous and oil phases, U_{water}/U_{oil}, from 1 to 12 results in generation of 1.3 pL to 4.6 pL aqueous plugs segmented by 1.5 pL to 0.4 pL oil droplets (Fig. 4C). Droplet frequency is critical to define the ultimate time resolution of neurochemical sensing.[14,20,22] Frequency varies between 1.2 Hz to 6.7 Hz with the increase of U_{water}/U_{oil} (Fig. 4D). Both the aqueous plug volume and the frequency scale linearly with flow rate ratio, which is expected for the squeezing regime.[35,37]

Electrospray-assisted phase separation

For visualization and profiling of electrospray plumes, a 3 mW 532 nm laser light was collimated and projected onto the nESI emitter nozzle and the electrosprayed plume. Fig. 5 shows a series of consecutive single-frame images from videos recorded in a fluorescence microscope for silicon chips with design 1 (Fig. 5A and B), design 2 (Fig. 5D and E), and design 3 (Fig. 5G and H). Leftmost (Fig. 5A, D and G) and rightmost (Fig. 5B, E and H) images correspond to the electrospraying of aqueous plugs and oil droplets within a single spraying cycle, correspondingly.

For the symmetric sharpened tip nozzle of design 1 (Fig. 5A–C), electrospraying of both aqueous phase (Fig. 5A) and oil phase (Fig. 5B) results in a single narrow (less than 50 μm lateral spread over 1 mm distance) central plume. Its density, as attested by the intensity of scattered laser light (measured at the blue bar monitor in Fig. 5A), is almost constant for both

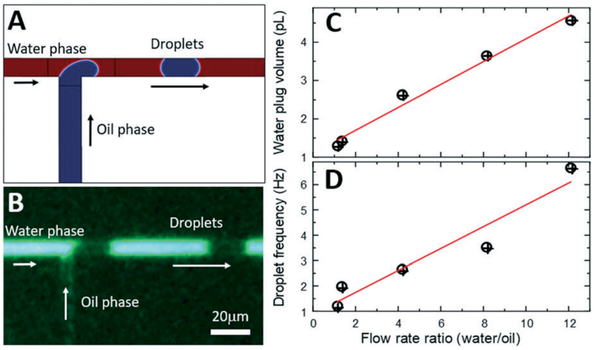

Fig. 4 On-chip generation of oil-segmented aqueous flow. A) Numerical COMSOL simulation of droplet generation in the squeezing regime. B) Fluorescent microscope image of the water plugs (green) segmented by octanol (dark) droplets at the T-junction of microfluidic channels in a squeezing regime. C). Measured aqueous plug volume as a function of the water/oil flow rate ratio. D) Measured droplet frequency as a function of the water/oil flow rate ratio.

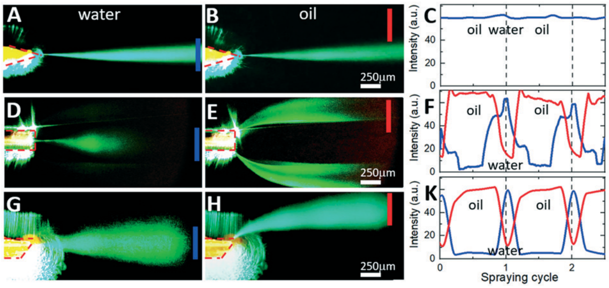

Fig. 5 Spatial and temporal separation of aqueous and oil phases during electrospraying. Single-frame images of a video of the electrosprayed plume for two consecutive phases of a spraying cycle. Images A, D and G correspond to the water electrospraying cycle, while B, E and H correspond to the oil phase electrospraying cycle. Rows (A and B), (D and E), and (G and H) correspond to different nozzle tip designs 1, 2, and 3, correspondingly. Intensity of light scattered off of an electrosprayed plume within a monitor area (blue and red bars) is shown in C, F, and K for different nozzle tip designs 1, 2, and 3, correspondingly.

aqueous and oil spray cycles (blue line in Fig. 5C). There is no light detected outside of the central plume (measured by the off-center red monitor in Fig. 5B). Such behaviour is expected from the modelling results of Fig. 2A and D since the electric field strength at the single "hot spot" on the outlet orifice of the emitter exceeds the initiation thresholds for effective electrospraying of both aqueous and oil phases. Moving the "hot spots" away from the outlet orifice as in the flat-end nozzle of design 2 (Fig. 2B and E) results in repetitive switching of the position, angle, and divergence of the plume across the spraying cycle (Fig. 5D–F). While the aqueous phase is sprayed in a single central plume directly at the nozzle orifice (Fig. 5D), the oil phase spreads towards the flat-end nozzle corners forming two off-center plumes (Fig. 5E). Corresponding temporal traces of scattered light intensity monitored at the center (blue monitor) and at the edge (red monitor) illustrate periodic switching between the off-center plumes and the central plume with a period of the droplet-segmented flow (Fig. 5F). The observed spatial and temporal separation of aqueous and oil phases was as expected by our intuitive model of Fig. 2G. While the aqueous phase forms a cone-jet electrospray at the very moment of being ejected from the nozzle with a relatively low electric field strength, the oil phase with a higher Taylor cone initiation threshold forms a cone-jet only after spreading towards the "hot spots" at the nozzle edges.

Such interpretation is validated by the spatial and temporal electrospray pattern observed in the case of design 3 (Fig. 2C and F) with its angled nozzle tip (Fig. 5G–K). While the aqueous phase is sprayed as a central plume (Fig. 5G) similar to other designs, the oil phase is sprayed from the sharp end of the nozzle at almost 45° with no indication of another plume at the opposite obtuse nozzle edge (Fig. 5H). Temporal switching between the central aqueous plume and off-center oil plume is illustrated in (Fig. 5K), as the scattered light intensity measured in the frame center (blue) and at its edge (red) switches out of phase with the periodicity of the segmented flow.

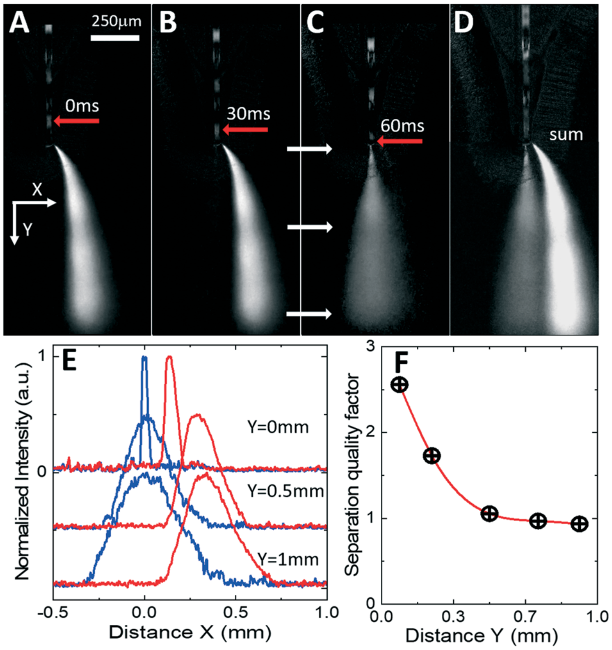

Fig. 6 Phase separation efficiency. A)–C) Consecutive single-frame background-subtracted images during the oil phase (A and B) and the aqueous phase (C) of the spraying cycle. Red arrows in A)–C) are showing the location of the same aqueous plug droplet for corresponding time frames. D) Frame-averaged background-subtracted image of the electrospray showing spatial separation of the center and the off-center plumes. Magnification and coordinates in A)–D) are the same. E) Intensity profiles of the aqueous (blue) and oil (red) plumes at various *Y* distances from the nozzle edge as shown by white arrows in C). F) Quality factor of phase separation efficiency.

To correlate the movement of oil-segmented flows and formation of electrosprayed plumes, an aqueous phase was fluorescently labelled with fluorescein (Sigma-Aldrich), and oil phase with Rhodamine B (Sigma-Aldrich). Fluorescent labelling enables time tracking of the droplets towards the nozzle and identification of precise timing of plume switching. To remove intense but stationary laser speckle scattering from the images (see Fig. 5), the stationary background image has been subtracted from each frame resulting in a series of consecutive greyscale images in Fig. 6A–C (see also the video provided in the ESI†). Droplet tracking (red arrows in Fig. 6A–C) confirms that the off-center plume is formed when the oil droplet is electrosprayed (Fig. 6A and B), while the central plume occurs when the aqueous phase is sprayed at the nozzle (Fig. 6C). When time-averaged (Fig. 6D), the resulting background-subtracted image shows both plumes well-separated even at mm-scale distances from the nozzle. To quantify this spatial separation, Fig. 6E shows normalized scattered light intensity profiles measured at different distances from the nozzle edge from images of Fig. 6B and C. Both plumes exhibit similar divergence from the initial full width at half-maximum values (W_a for the aqueous phase and W_o for oil phase) of less than 100 μm at the nozzle edge to 350 μm at a distance of 0.5 mm from the nozzle. Their spatial separation distance *D* increases from an initial 70 μm at the nozzle tip to 200 μm at a 0.5 mm distance (Fig. 6E). The efficiency of the phase separation can be estimated as a quality factor $Q = 2D/(W_a + W_o)$ shown in Fig. 6F, that exhibits an initial drop from 2.5 to 1 within the first 0.5 mm and then stabilization for longer distances up to 1 mm and beyond. Hence the spatial separation of the aqueous and oil phases is comparable to the diameters of the inlet capillaries typically used in ESI mass spectrometers, and this separation is maintained over mm-scale distances at which typical nESI emitters are located for efficient analyte ionization.

Hyphenation to mass spectrometry

To demonstrate the performance of our integrated silicon microfluidic platform in action, the integrated chip with the design 1 nozzle was placed at 2 mm distance from an

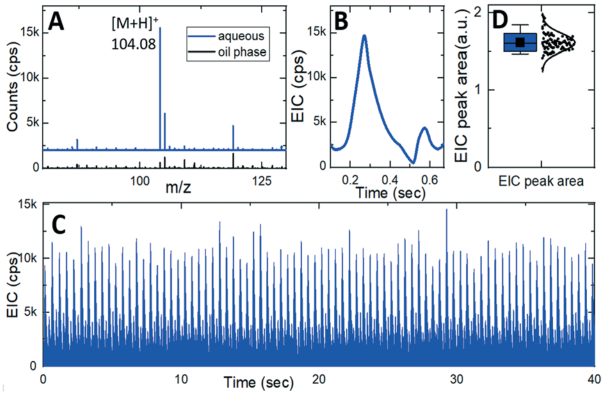

Fig. 7 Hyphenation to mass spectrometry. A) Mass spectra for electrosprayed aqueous phase (blue) and oil phase (black) around [GABA + H]$^+$ ion signal at 104.08 *m*/*z*. B) EIC of the intensity of *m*/*z* 104.08 signal during a single aqueous spraying cycle containing just 110 amol of GABA. C) 40 seconds EIC recording of electrosprayed segmented flow. D) Descriptive statistics of the EIC peaks area for data in C).

orifice of the ultrahigh-resolution quadrupole time-of-flight tandem mass spectrometer (maXis4G Bruker). The mass spectrometer was operated as described previously when used for capillary electrophoresis[38] except that the capillary holder was replaced by the integrated device, with the exact placement of the emitter monitored using an attached video camera. The aqueous phase (10 μM gamma aminobutyric acid (GABA) in DI water, Sigma-Aldrich) was segmented into 11 pL plugs separated by oil phase droplets (Fluorinert FC-40, Sigma-Aldrich).

Fig. 7A shows mass spectra measured during the electrospraying of the segmented flow of an oil phase (black curve) and aqueous phase (blue curve shifted up for clarity) exhibiting a characteristic peak of [GABA + H]$^+$ ions at *m*/*z* 104.08. Correspondingly, an extracted ion chromatogram (EIC) in Fig. 7B represents the intensity of [GABA + H]$^+$ ions during a spraying cycle of a single aqueous plug with just 110 amol of GABA. EIC peaks shape and intensity remains stable (Fig. 7C). Statistics of the peak area of 86 consecutive droplets (Fig. 7D) shows just 7% relative standard deviation (RSD). The limit of detection (LOD) was estimated from the mean value and the RSD of the EIC peaks approaching a few tens of attomoles.

Conclusions

Here we developed a silicon platform technology that enables on-chip integration of scaled-down microfluidic channels, a miniaturized T-junction droplet generator, and an n-ESI emitter for efficient delivery of analytes to subsequent online mass spectrometry analysis. Engineering of the emitter nozzle geometry enables control of the location of electric field "hot spots" relative to the microfluidic channel outlet. This unique feature enables effective spatial and temporal separation of electrosprayed oil and aqueous phases of the segmented flow. Operating in a cone-jet regime, the silicon integrated platform enables detection of GABA content in pL-scale droplets with high stability. Measurements of detection limits indicates an LOD at the mid-amol-level. The further development of this platform will enable droplet-by-droplet MS analysis with increased chemical sensitivity for detection of several important neurochemicals with high temporal and chemical resolution.

Conflicts of interest

There are no conflicts to declare.

Acknowledgements

Research reported in this publication was supported in part by the NINDS of the NIH grant UF1NS107677. The content is solely the responsibility of the authors and does not necessarily represent the official views of the National Institutes of Health.

Notes and references

1 E. M. Payne, D. A. Holland-Moritz, S. Sun and R. T. Kennedy, High-throughput screening by droplet microfluidics: Perspective into key challenges and future prospects, *Lab Chip*, 2020, **20**(13), 2247.
2 R. Beulig, R. Warias, J. Heiland, S. Ohla, K. Zeitler and D. Belder, A droplet-chip/mass spectrometry approach to study organic synthesis at nanoliter scale, *Lab Chip*, 2017, **17**(11), 1996.
3 M. Schirmer, K. Wink, S. Ohla, D. Belder, A. Schmid and C. Dusny, Conversion efficiencies of a few living microbial cells detected at a high throughput by droplet-based ESI-MS, *Anal. Chem.*, 2020, **92**(15), 10700.
4 Y. Zhou, Z. Chen, J. Zeng, J. Zhang, D. Yu, B. Zhang, X. Yan, L. Yang and Q. Wang, Direct Infusion ICP-q MS of Lined-up Single-Cell Using an Oil-Free Passive Microfluidic System, *Anal. Chem.*, 2020, **92**(7), 5286.
5 X. W. Diefenbach, I. Farasat, E. D. Guetschow, C. J. Welch, R. T. Kennedy, S. Sun and J. C. Moore, Enabling biocatalysis by high-throughput protein engineering using droplet microfluidics coupled to mass spectrometry, *ACS Omega*, 2018, **3**(2), 1498.
6 J. Ji, L. Nie, L. Qiao, Y. Li, L. Guo, B. Liu, P. Yang and H. H. Girault, Proteolysis in microfluidic droplets: an approach to interface protein separation and peptide mass spectrometry, *Lab Chip*, 2012, **12**(15), 2625.
7 S. Sun and R. T. Kennedy, Droplet electrospray ionization mass spectrometry for high throughput screening for enzyme inhibitors, *Anal. Chem.*, 2014, **86**(18), 9309.
8 E. E. Kempa, C. A. Smith, X. Li, B. Bellina, K. Richardson, S. Pringle, J. L. Galman, N. J. Turner and P. E. Barran, Coupling droplet microfluidics with mass spectrometry for ultrahigh-throughput analysis of complex mixtures up to and above 30 Hz, *Anal. Chem.*, 2020, **92**(18), 12605.
9 D.-Q. Jin, S.-W. Shi, Y. Ma and Q. Fang, LC-Swan probe: an integrated in situ sampling interface for liquid chromatography separation and mass spectrometry analysis, *Anal. Chem.*, 2020, **92**(13), 9214.

10 F. G. Pinto, I. Mahmud, T. A. Harmon, V. Y. Rubio and T. J. Garrett, Rapid Prostate Cancer Noninvasive Biomarker Screening Using Segmented Flow Mass Spectrometry-Based Untargeted Metabolomics, *J. Proteome Res.*, 2020, **19**(5), 2080.

11 D. A. Beard, Taylor dispersion of a solute in a microfluidic channel, *J. Appl. Phys.*, 2001, **89**(8), 4667.

12 M. Wang, G. T. Roman, K. Schultz, C. Jennings and R. T. Kennedy, Improved temporal resolution for in vivo microdialysis by using segmented flow, *Anal. Chem.*, 2008, **80**(14), 5607.

13 M. Wang, T. Slaney, O. Mabrouk and R. T. Kennedy, Collection of nanoliter microdialysate fractions in plugs for off-line in vivo chemical monitoring with up to 2 s temporal resolution, *J. Neurosci. Methods*, 2010, **190**(1), 39.

14 R. T. Kennedy, Emerging trends in in vivo neurochemical monitoring by microdialysis, *Curr. Opin. Chem. Biol.*, 2013, **17**(5), 860.

15 W. H. Lee, T. R. Slaney, R. W. Hower and R. T. Kennedy, Microfabricated sampling probes for in vivo monitoring of neurotransmitters, *Anal. Chem.*, 2013, **85**(8), 3828.

16 T. R. Slaney, J. Nie, N. D. Hershey, P. K. Thwar, J. Linderman, M. A. Burns and R. T. Kennedy, Push–pull perfusion sampling with segmented flow for high temporal and spatial resolution in vivo chemical monitoring, *Anal. Chem.*, 2011, **83**(13), 5207.

17 M. Wang, N. D. Hershey, O. S. Mabrouk and R. T. Kennedy, Collection, storage, and electrophoretic analysis of nanoliter microdialysis samples collected from awake animals in vivo, *Anal. Bioanal. Chem.*, 2011, **400**(7), 2013.

18 M. Perry, Q. Li and R. T. Kennedy, Review of recent advances in analytical techniques for the determination of neurotransmitters, *Anal. Chim. Acta*, 2009, **653**(1), 1.

19 J. Pei, Q. Li, M. S. Lee, G. A. Valaskovic and R. T. Kennedy, Analysis of samples stored as individual plugs in a capillary by electrospray ionization mass spectrometry, *Anal. Chem.*, 2009, **81**(15), 6558.

20 T. Ngernsutivorakul, D. J. Steyer, A. C. Valenta and R. T. Kennedy, In vivo chemical monitoring at high spatiotemporal resolution using microfabricated sampling probes and droplet-based microfluidics coupled to mass spectrometry, *Anal. Chem.*, 2018, **90**(18), 10943.

21 P. Song, N. D. Hershey, O. S. Mabrouk, T. R. Slaney and R. T. Kennedy, Mass spectrometry "sensor" for in vivo acetylcholine monitoring, *Anal. Chem.*, 2012, **84**(11), 4659.

22 T. Ngernsutivorakul, T. S. White and R. T. Kennedy, Microfabricated probes for studying brain chemistry, *ChemPhysChem*, 2018, **19**(10), 1128.

23 L. M. Fidalgo, G. Whyte, B. T. Ruotolo, J. L. Benesch, F. Stengel, C. Abell, C. V. Robinson and W. T. Huck, Coupling microdroplet microreactors with mass spectrometry: reading the contents of single droplets online, *Angew. Chem.*, 2009, **121**(20), 3719.

24 R. T. Kelly, J. S. Page, I. Marginean, K. Tang and R. D. Smith, Dilution-free analysis from picoliter droplets by nano-electrospray ionization mass spectrometry, *Angew. Chem.*, 2009, **121**(37), 6964.

25 Y. Zhu and Q. Fang, Integrated droplet analysis system with electrospray ionization-mass spectrometry using a hydrophilic tongue-based droplet extraction interface, *Anal. Chem.*, 2010, **82**(19), 8361.

26 M. Wang, G. T. Roman, M. L. Perry and R. T. Kennedy, Microfluidic chip for high efficiency electrophoretic analysis of segmented flow from a microdialysis probe and in vivo chemical monitoring, *Anal. Chem.*, 2009, **81**(21), 9072.

27 Q. Li, J. Pei, P. Song and R. T. Kennedy, Fraction collection from capillary liquid chromatography and off-line electrospray ionization mass spectrometry using oil segmented flow, *Anal. Chem.*, 2010, **82**(12), 5260.

28 P. N. Nge, C. I. Rogers and A. T. Woolley, Advances in microfluidic materials, functions, integration, and applications, *Chem. Rev.*, 2013, **113**(4), 2550.

29 B. Legrand, A. E. Ashcroft, L. Buchaillot and S. Arscott, SOI-based nanoelectrospray emitter tips for mass spectrometry: a coupled MEMS and microfluidic design, *J. Micromech. Microeng.*, 2007, **17**(3), 509.

30 W. Kim, M. Guo, P. Yang and D. Wang, Microfabricated monolithic multinozzle emitters for nanoelectrospray mass spectrometry, *Anal. Chem.*, 2007, **79**(10), 3703.

31 S. Yadavali, D. Lee and D. Issadore, Robust Microfabrication of Highly Parallelized Three-Dimensional Microfluidics on Silicon, *Sci. Rep.*, 2019, **9**(1), 1.

32 Y. Zhang, A. Esters, O. Bi and Y. Vlasov, 2019 20th International Conference on Solid-State Sensors, Actuators and Microsystems & Eurosensors XXXIII (TRANSDUCERS & EUROSENSORS XXXIII), 2019, p. 209.

33 L. Sainiemi, T. Nissilä, R. Kostiainen, S. Franssila and R. A. Ketola, A microfabricated micropillar liquid chromatographic chip monolithically integrated with an electrospray ionization tip, *Lab Chip*, 2012, **12**(2), 325.

34 M. J. D. Boer, R. W. Tjerkstra, J. W. Berenschot, H. V. Jansen, G. J. Burger, J. G. E. Gardeniers, M. Elwenspoek and A. V. D. Berg, Micromachining of buried micro channels in silicon, *J. Microelectromech. Syst.*, 2000, **9**(1), 94.

35 P. Garstecki, M. J. Fuerstman, H. A. Stone and G. M. Whitesides, Formation of droplets and bubbles in a microfluidic T-junction—scaling and mechanism of break-up, *Lab Chip*, 2006, **6**(3), 437.

36 K. Tang, J. S. Page and R. D. Smith, Charge competition and the linear dynamic range of detection in electrospray ionization mass spectrometry, *J. Am. Soc. Mass Spectrom.*, 2004, **15**(10), 1416.

37 P. Zhu and L. Wang, Passive and active droplet generation with microfluidics: a review, *Lab Chip*, 2017, **17**(1), 34.

38 J. T. Aerts, K. R. Louis, S. R. Crandall, G. Govindaiah, C. L. Cox and J. V. Sweedler, Patch clamp electrophysiology and capillary electrophoresis–mass spectrometry metabolomics for single cell characterization, *Anal. Chem.*, 2014, **86**(6), 3203.